Research Square

Preprints are preliminary reports that have not undergone peer review.
They should not be considered conclusive, used to inform clinical practice,
or referenced by the media as validated information.

Exposure and capacity mismatch shapes multihazard adaptation priorities for older adults in the Yangtze Delta

Qi Wu
Anhui Institute of Information Technology
Peijun Lu
lupj@mail.tsinghua.edu.cn
Tsinghua University
Shun Huang
Suzhou Polytechnic Institute of Agriculture
Wei Wang
Hunan City University
Mingjing Ding
Anhui Jianzhu University

Article

Keywords:

Posted Date: November 4th, 2026

DOI: https://doi.org/10.21203/rs.3.rs-11020456/v1

License: This work is licensed under a Creative Commons Attribution 4.0 International License.
Read Full License

Additional Declarations: No competing interests reported.

Exposure and capacity mismatch shapes multihazard adaptation priorities for older adults in the Yangtze Delta

Authors: Qi Wu[1] and Peijun Lu[2]*, Shun Huang[3]*, Wei Wang[4], Mingjing Ding[5]

[1] School of Art and Design, Anhui Institute of Information Technology, Wanzhi District, Wuhu, Anhui, China 241000;
[2] School of Architecture, Tsinghua University, Haidian District, Beijing, China 100084
[3] School of Landscape Architecture, Suzhou Polytechnic Institute of Agriculture, Gusu District, Suzhou, Jiangsu, China 215008
[4] College of Architecture & Urban Planning, Hunan City University, Yiyang, Hunan, China 413000
[5] College of Design and Innovation, Anhui Jianzhu University, Hefei, Anhui, China 230000
*Corresponding author: lupj@mail.tsinghua.edu.cn；huangs@szai.edu.cn

Abstract

Climate extremes threaten older adults unevenly because hazards, ageing and adaptive capacity are spatially mismatched. Here we develop EDGE, an equity-driven framework that quantifies multi-hazard exposure in aggregate and per-resident terms, diagnoses county-level healthcare-capacity mismatch, and derives the marginal benefit of added capacity analytically rather than by curve fitting. Applied to 201 counties in the Yangtze River Delta under four SSP pathways and five CMIP6 models, EDGE shows that elderly multi-hazard burden peaks in 2050–2075, when it rises 195% above baseline under SSP3-7.0. Counties with more advanced ageing hold systematically fewer hospital beds per older resident (Spearman $\rho = -0.47$), a persistent counter-need allocation. Marginal benefit is highest where high exposure intensity and low capacity coincide, concentrated in southern Anhui and northern Jiangsu: ensemble-mean returns in the priority group are 1.85 times those in the over-resourced group, and this ordering holds under every pathway and at any attenuation strength. Directing incremental healthcare investment there is a no-regret strategy.

Introduction

Climate change and rapid population ageing are converging to reshape the geography of health risk. Global warming is increasing the frequency, intensity, and co-occurrence of extreme precipitation, heatwaves, and tropical-cyclone winds, while the global population aged 65 and over continues to grow rapidly, with China ageing faster than almost any other large economy[1,2]. These two trends interact: intensifying extreme events and their co-occurrence pose an accelerating threat to health, and older adults are among the most affected[3–5]. Exposure to compound extreme events has risen markedly in recent years, particularly in China's most aged regions, such as the Yangtze River basin and the Bohai Sea Rim[6].

Older adults are consistently identified as a high-sensitivity population in climate–health assessments[7,8]. Physiological heat sensitivity, high chronic-disease prevalence, reduced mobility, social

isolation, and reliance on timely medical care can all amplify the consequences of heat, flooding, wind disruption, and emergency-service delay[9–12]. In multi-hazard environments, these vulnerabilities compound one another: extreme heat, typhoons, and heavy rainfall can simultaneously worsen pre-existing conditions, impair physical function, and delay rescue and treatment, producing mortality rates substantially higher than in the general population[13–15]. Yet the climate risk faced by older adults is not determined by hazard intensity alone. It emerges from the spatial intersection of physical hazard, demographic exposure, social vulnerability, and the adaptive resources that allow communities and health systems to absorb shocks[16–18]. A county with moderate hazard intensity but a large older population and weak healthcare capacity may therefore face a greater planning burden than a county with higher hazard intensity but greater adaptive resources.

This distinction is especially important in fast-urbanizing delta regions, where hazards, demographic change, and public-service provision are strongly uneven. Delta urban agglomerations combine coastal and fluvial exposure, high population density, steep rural–urban gradients, and large differences in fiscal and healthcare capacity, making them sensitive not only to individual hazards but also to compound events in which heat, heavy rainfall, and typhoon winds interact with infrastructure disruption and constrained service access[19–23]. The Yangtze River Delta Urban Agglomeration (YRDUA) is an instructive case: economically advanced at the regional scale yet internally heterogeneous[20,24], spanning Shanghai and county-level units across Jiangsu, Zhejiang, and Anhui, where future hazards under different SSP pathways and the uneven distribution of healthcare resources and older residents coincide[25]. This risk is not hypothetical: in August 2026 Typhoon Dolphin struck the Zhejiang coast and tracked slowly inland across the YRDUA, where 24-h rainfall of 300–425 mm—Shanghai's heaviest since 1951—coincided with damaging winds, waterlogging and suspended transport. Such compound, inland-reaching episodes disrupt access to care far beyond the coastal cores[26].

Despite growing attention to climate–health risk, three gaps remain. First, climate-risk assessments often prioritize hazard exposure, whereas health-system planning typically evaluates resources through administrative supply indicators such as bed counts[27–29]; the two are rarely integrated within a single spatial framework. Second, existing studies tend to analyse each dimension—multi-hazard exposure, healthcare adaptive capacity, residual burden, and marginal benefit—in isolation, leaving the equity-relevant relationships among them unexamined[30,31]. Third, even where exposure and resources are mapped together, neither an exposure map nor a service-supply map indicates where an additional unit of adaptive capacity should be placed to reduce burden most effectively. Together, these gaps point to the absence of a systematic, equity-driven framework that links the dimensions of elderly multi-hazard risk and supports allocation decisions.

Addressing these gaps requires linking exposure and capacity without conflating them. Physical multi-hazard exposure measures where older adults encounter climate stressors. Healthcare adaptive capacity measures whether local systems hold resources that can reduce burden once exposure occurs. Residual burden represents the portion of projected burden that remains after capacity is accounted for. Marginal benefit then identifies where an additional unit of healthcare capacity or investment yields the greatest reduction in residual burden[32]. Separating these quantities is essential: hospital beds cannot prevent heavy rainfall, heatwaves, or typhoon winds, but they can shape emergency response, treatment capacity, and a system's ability to absorb climate-sensitive demand.

Here we develop EDGE, an Equity-Driven Guidance framework for Elderly climate adaptation (Fig. 1). Its contribution is not another single-hazard exposure index, but the integration of three elements usually analysed separately: multi-hazard exposure, healthcare-capacity mismatch, and the marginal benefit of added capacity.

EDGE proceeds in three steps. Step 1 (MEASURE) couples extreme-precipitation, heatwave and typhoon-wind indices into a multi-hazard co-occurrence index (HI). Weighting HI by the older population shows where compound exposure (B) concentrates; dividing B by that population gives the exposure intensity (h) borne by an average older resident. Step 2 (DIAGNOSE) tests whether the distribution of healthcare resources matches demographic and exposure need, and classifies counties into exposure–capacity typologies. Step 3 (GUIDE) estimates the marginal benefit (MB) of an additional unit of adaptive capacity (C) in reducing modelled residual burden (R), and how this benefit shifts across emission scenarios. This sequence converts climate-risk assessment from a descriptive mapping exercise into an allocation-oriented framework that identifies where adaptation resources are most needed and where incremental capacity is most beneficial under each scenario.

We apply EDGE to 201 county-level units across the YRDUA using five CMIP6 models, four SSP scenarios, and three future periods relative to a 2015–2025 baseline. By linking compound-event climate science with health-equity and service-access concepts[33,34], the analysis provides a decision-support basis—rather than an epidemiological attribution—for identifying counties where elderly climate exposure and healthcare deficit coincide, and for evaluating scenario-specific returns to additional capacity. It thus advances a practical form of climate–health adaptation evidence: identifying not only who is exposed, but where system capacity is insufficient and where incremental investment may most reduce modelled burden.

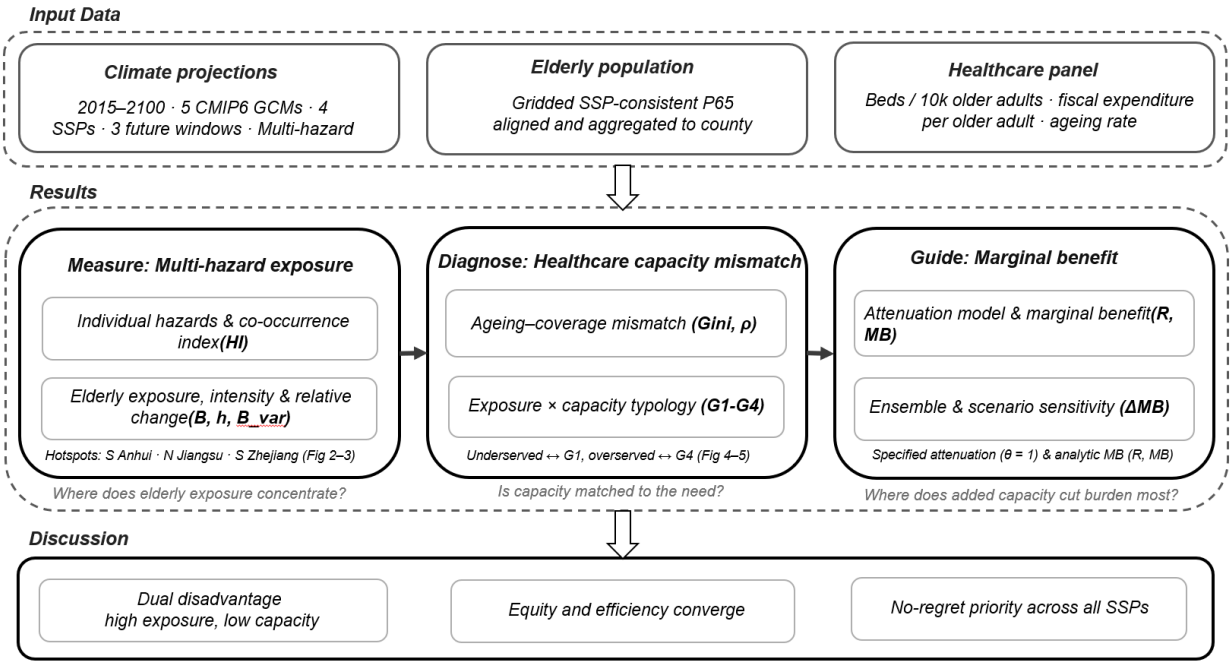


Fig. 1 The EDGE framework of the YRDUA.

The framework proceeds in three steps applied to county-level units of the Yangtze River Delta Urban Agglomerations. Inputs comprise CMIP6 projections (2015–2100; five GCMs; four SSPs; three future windows against a 2015–2025 baseline), gridded population aged ≥65 (P65), and a county healthcare panel (2012–2022). MEASURE couples extreme-precipitation, heatwave and typhoon-wind indices into a multi-hazard index (HI) and weights it by P65 to obtain elderly exposure (B) and its relative change (B_{var}) (Figs. 2–3). DIAGNOSE tests whether capacity matches need and classifies counties into four exposure–capacity typologies (G1–G4) (Figs. 4–5). GUIDE specifies the attenuation of residual burden (R) by adaptive capacity (C) and derives the marginal benefit of added capacity (MB) analytically, together with its emission sensitivity (ΔMB) (Figs. 6–7). Together the steps identify where added capacity most reduces residual burden.

Results

Future elderly multi-hazard exposure intensifies and shifts inland

We assessed future changes in elderly multi-hazard exposure across the YRDUA. Exposure is the product of the gridded elderly population (aged ≥65) and a multi-hazard co-occurrence index (HI) that couples extreme-precipitation, heatwave and typhoon-wind hazards at each grid cell (Methods). We projected exposure under four Shared Socioeconomic Pathways (SSP1-2.6, SSP2-4.5, SSP3-7.0, and SSP5-8.5) across three future periods (2025–2050, 2050–2075, and 2075–2100), relative to a 2015–2025 baseline, using five CMIP6 models to capture inter-model uncertainty.

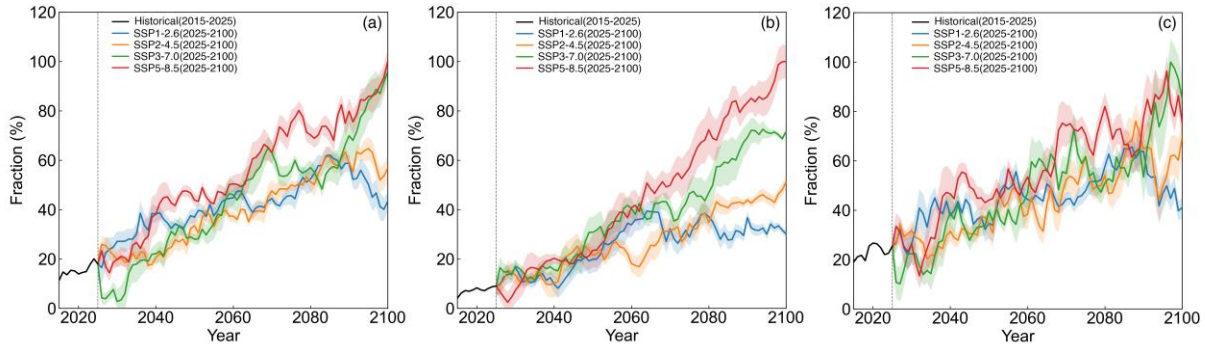


Fig. 2 Projected temporal evolution of individual climate hazard exposure across the YRDUA under four SSP scenarios (2015–2100).

(a) Extreme precipitation exposure index; (b) Heatwave exposure index; (c) Typhoon wind exposure index. Shaded bands indicate inter-model uncertainty. The vertical dashed line marks the 2025 divergence point between the historical and scenario periods.

The three hazards follow markedly different temporal trajectories (Fig. 2) and correspondingly different spatial patterns of change (Supplementary Figs. 1–3). Extreme precipitation and heatwave exposure rise monotonically, and the four scenarios diverge clearly after 2025 (Fig. 2a, b): the precipitation signal is spatially fragmented and concentrates over built-up, low-permeability surfaces (Supplementary Fig. 1), whereas heatwave intensification is near region-wide and reaches its greatest amplitude inland under the high-emission pathways by 2075–2100 (Supplementary Fig. 2). This riseThis rise is steepest for heatwave exposure, which increases by 100% under SSP5-8.5 by 2100 but by only

30% under SSP1-2.6 (Fig. 2b). Typhoon-wind exposure, by contrast, oscillates, and the highest-emission scenario does not produce the greatest exposure (Fig. 2c; Supplementary Fig. 3), reflecting the sensitivity of tropical cyclones to atmospheric circulation rather than to warming alone. Because these hazards move in different directions, any single-hazard assessment would misrepresent the compound risk faced by older adults—motivating the multiplicative form of HI.

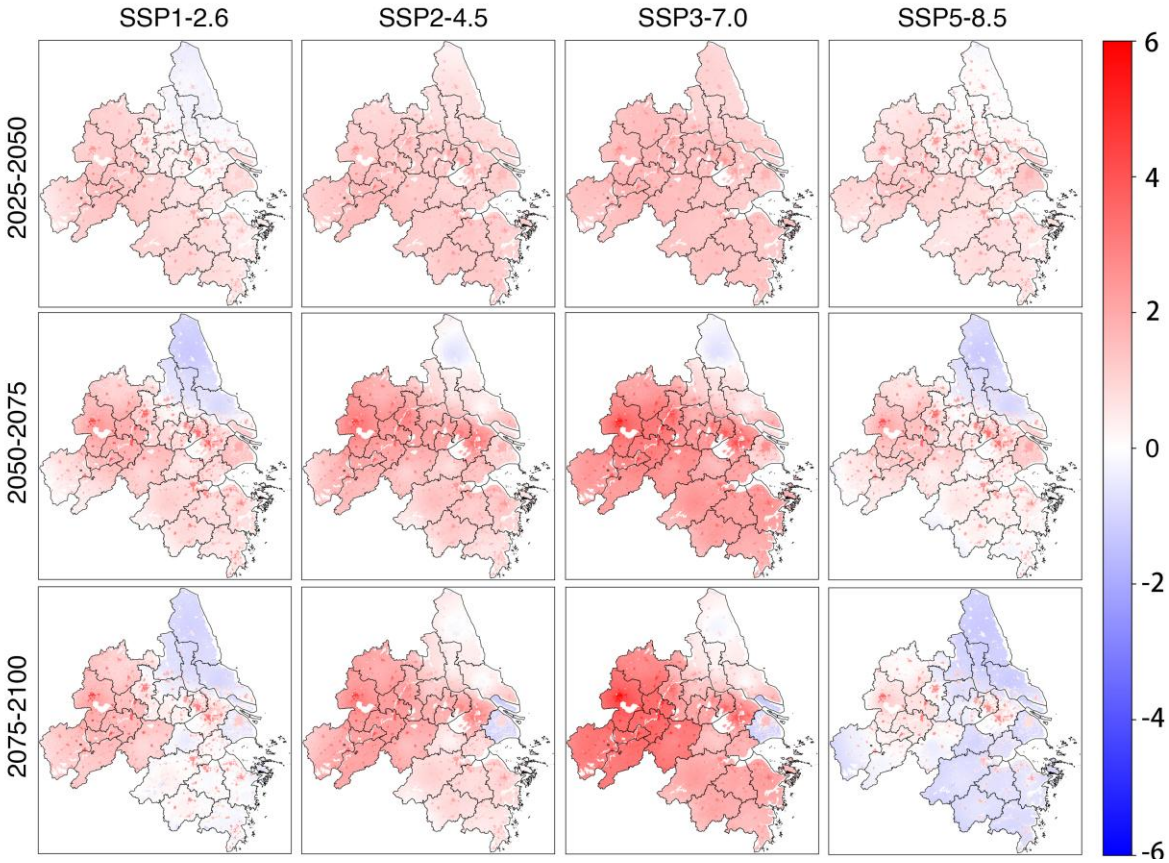


Fig. 3 Relative change in projected multi-hazard exposure of older adults (aged ≥65) under future climate scenarios.

Columns show SSP1-2.6, SSP2-4.5, SSP3-7.0 and SSP5-8.5; rows show periods 2025–2050, 2050–2075 and 2075–2100. Colour scale displays the signed-log transform of, B-var., which integrates compound hazard co-occurrence with the elderly population; red indicates increase, blue indicates decrease.

Table 1. Projected changes in elderly multi-hazard exposure in the YRDUA across four SSP scenarios and three future periods.

Scenario	Period	Mean B ($\times 10^3$)	Max B ($\times 10^3$)	Exposure growth rate (%)[a]	Positive-change counties (%)	Hotspot counties (n)[b]
SSP1-2.6	2025–2050	61.5	852.7	69.2	99.4	24
	2050–2075	86.9	1161.5	139.2	94.5	98
	2075–2100	73.8	904.1	103.1	93.0	72

SSP2-4.5	2025–2050	70.9	1008.5	91.3	100.0	37
	2050–2075	84.4	1103.3	127.8	98.0	108
	2075–2100	71.7	789.0	93.5	98.5	90
SSP3-7.0	2025–2050	64.9	889.4	97.8	100.0	43
	2050–2075	96.6	1225.2	194.8	98.0	172
	2075–2100	81.9	831.8	150.0	99.0	141
SSP5-8.5	2025–2050	78.9	1218.3	97.2	100.0	35
	2050–2075	92.5	1326.5	131.2	95.0	77
	2075–2100	65.5	858.4	63.7	83.6	29

Population-weighted exposure intensifies over time and concentrates in the less-developed inland counties of the region (Fig. 3, Table 1). Mean exposure peaks during 2050–2075 under every scenario and is highest under SSP3-7.0, which shows the largest increase relative to baseline (+195%) and the largest number of affected counties (172 of 201; Table 1). Hotspots across southern Anhui, northern Jiangsu and southern Zhejiang persist across all scenarios, indicating that the geography of elderly exposure is largely insensitive to the emission pathway. By 2075–2100, exposure declines under SSP5-8.5 (+64%, the lowest of all scenarios), and several eastern coastal counties show reduced exposure—both consistent with the non-monotonic typhoon signal in Fig. 2c and with the coastal concentration of typhoon-wind change in Supplementary Fig. 3.

Two factors jointly produce these hotspots: a growing elderly population (Supplementary Fig. 4) and intensifying multi-hazard co-occurrence (Fig. 3). Notably, the elderly population rises across most inland counties even where the total population is projected to decline (Supplementary Fig. 5), indicating that increasing exposure there is driven by demographic composition rather than by population growth. Where only one factor is present, exposure remains lower. Southern Anhui, northern Jiangsu, and southern Zhejiang combine rapidly ageing populations with rising multi-hazard co-occurrence, whereas the populous Shanghai–Suzhou–Hangzhou core has many older residents but comparatively modest hazard increases. HI captures only the three climate hazards considered here; the same inland uplands also contain the region's highest density of geological hazards (Supplementary Fig. 6), which lie outside the present scope but would add to the burden borne by several priority counties. This coincidence of demographic and hazard gradients drives the inland concentration of exposure, and raises a critical question: are healthcare resources allocated to match this concentrated and growing need? We address this in the next section.

Healthcare capacity is mismatched with demographic and exposure need

Having established where elderly exposure concentrates, we asked whether healthcare resources are distributed to match this need. We characterized each county by its hospital bed coverage (beds per 10,000 older residents) and ageing rate over 2012–2022, and tested their association across the YRDUA.

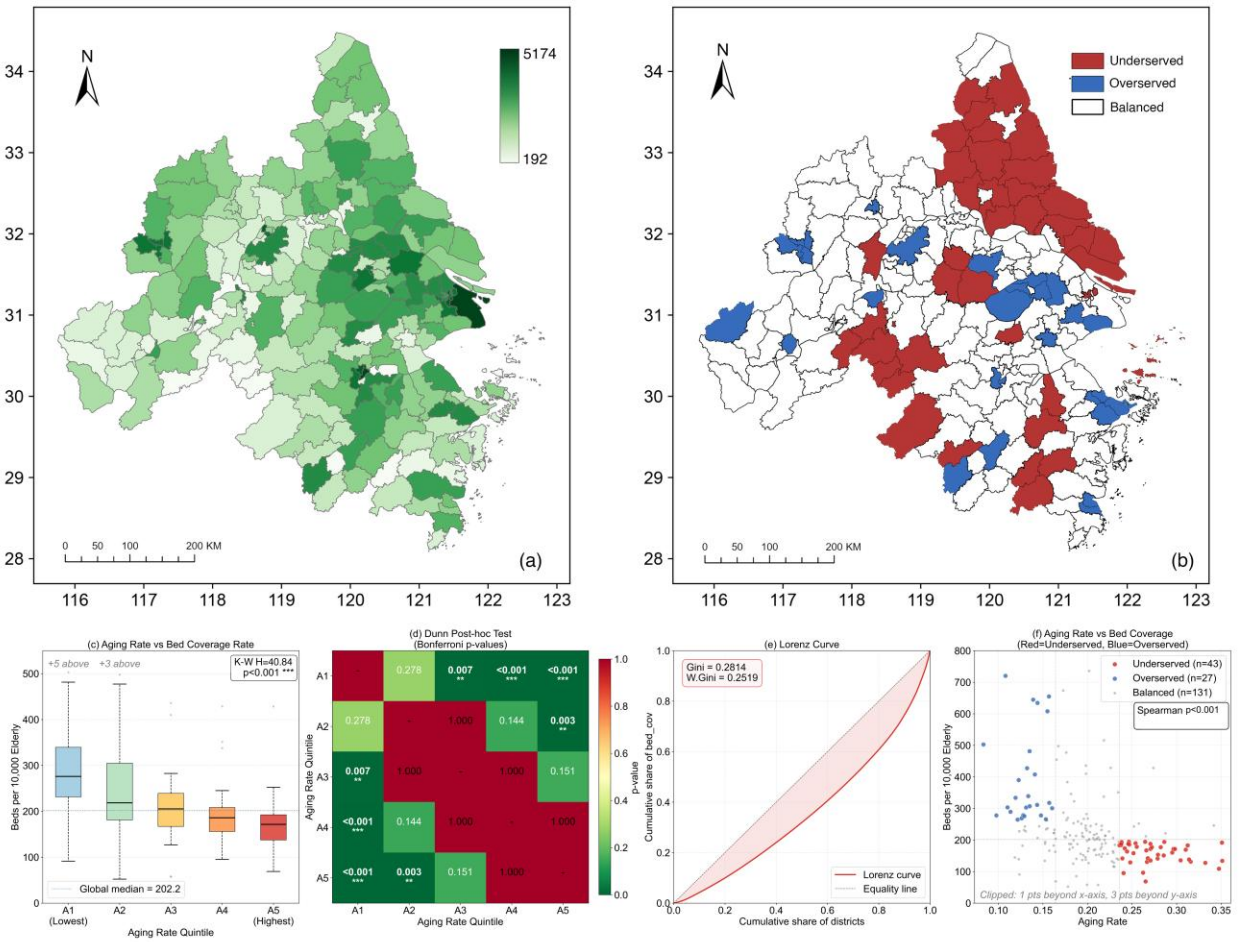


Fig. 4 Mismatch between healthcare resources and population ageing across the YRDUA (2012–2022).

(a) Spatial distribution of bed coverage. (b) Counties classified as underserved (high ageing, low coverage), overserved (low ageing, high coverage), or balanced. (c) Bed coverage by ageing-rate quintile (A1, lowest; A5, highest); dashed line marks the global median. (d) Dunn post-hoc pairwise p-values between quintiles. (e) Lorenz curve of bed-coverage inequality. (f) County-level association between ageing rate and bed coverage.

Bed coverage declines as ageing intensifies, revealing a counter-need allocation of healthcare resources (Fig. 4a, c, d). Counties in the lowest ageing quintile hold a median of 276 beds per 10,000 older residents, compared with 172 in the highest quintile (Fig. 4c). The gradient is statistically robust (Kruskal–Wallis $H = 40.84$, $df = 4$, $P = 2.9 \times 10^{-8}$, $\varepsilon^2 = 0.188$). Dunn post-hoc comparisons show that the least-aged quintile differs from A3, A4 and A5 (Bonferroni-adjusted $P = 0.007$, 3.1×10^{-5} and 5.1×10^{-8}) and that A2 differs from A5 ($P = 0.003$), whereas no adjacent quintile pair is separable (all $P \geq 0.278$; Fig. 4d); the decline is therefore monotonic across the ageing gradient but statistically resolvable only between quintiles sufficiently far apart. Bed coverage is unequally distributed across counties (Gini = 0.2814; population-weighted Gini = 0.2519; Fig. 4e), and ageing rate correlates negatively with coverage (Spearman $\rho = -0.470$, $P = 1.9 \times 10^{-10}$, 95% CI [−0.571, −0.355]; Fig. 4f). Mapping the two dimensions together identifies 43 underserved counties (high ageing, low coverage) coexisting with 27 overserved

counties (low ageing, high coverage) (Fig. 4b). The underserved counties form two clusters—southern Anhui and northern Jiangsu. The northern Jiangsu cluster coincides with the exposure hotspots of Fig. 3, whereas the southern Anhui cluster does not: these counties combine moderate exposure with the region's scarcest healthcare resources. The two geographies therefore overlap only partially, which is itself informative—neither an exposure map nor a service-supply map identifies the same set of counties, and the priority group emerges only when the two are considered jointly.

To translate this mismatch into an actionable structure, we classified counties by median splits of multi-hazard exposure intensity and adaptive capacity (Fig. 5a). Exposure intensity ($h = B/P65$) measures the hazard co-occurrence experienced by an average older resident, and the capacity index C combines bed coverage with fiscal expenditure per older resident; both are per-resident quantities and are therefore directly comparable. This yields G1 (high intensity, low capacity; n = 55), G2 (high intensity, high capacity; n = 46), G3 (low intensity, low capacity; n = 45) and G4 (low intensity, high capacity; n = 55).

G1 counties (the priority group) combine the highest exposure intensity (0.106) with the lowest capacity (C = 0.345), holding 160.8 beds per 10,000 older residents and 39,552 yuan of fiscal expenditure per older resident. G4 counties hold 2.4 times the bed coverage (384.2) and 1.9 times the fiscal expenditure per older resident (75,159) at the lowest exposure intensity (0.071; Table 2). This ordering reverses when exposure is measured as an aggregate rather than a rate: G4 counties, which contain the largest older populations, carry the highest total exposure and G1 the lowest. We therefore based the typology on exposure intensity, because adaptation resources are allocated per resident; aggregate exposure remains the appropriate metric for identifying where the greatest numbers of older adults are exposed (Fig. 3).

The typology is consistent with the diagnostic classification of Fig. 4 (Fig. 5b): 67.4% of underserved counties (29 of 43) fall into G1 and 70.4% of overserved counties (19 of 27) fall into G4. More informative is the absence of directional contradiction—no overserved county is classified as G1, and only one underserved county (2.3%) falls into G4. The two schemes share bed coverage as an input but differ on their remaining axes (ageing rate versus exposure intensity; bed coverage alone versus the composite capacity index), so their agreement reflects a substantive pattern rather than a definitional one. These dually disadvantaged counties raise the central policy question: where should limited healthcare investment be directed to reduce residual elderly burden most effectively?

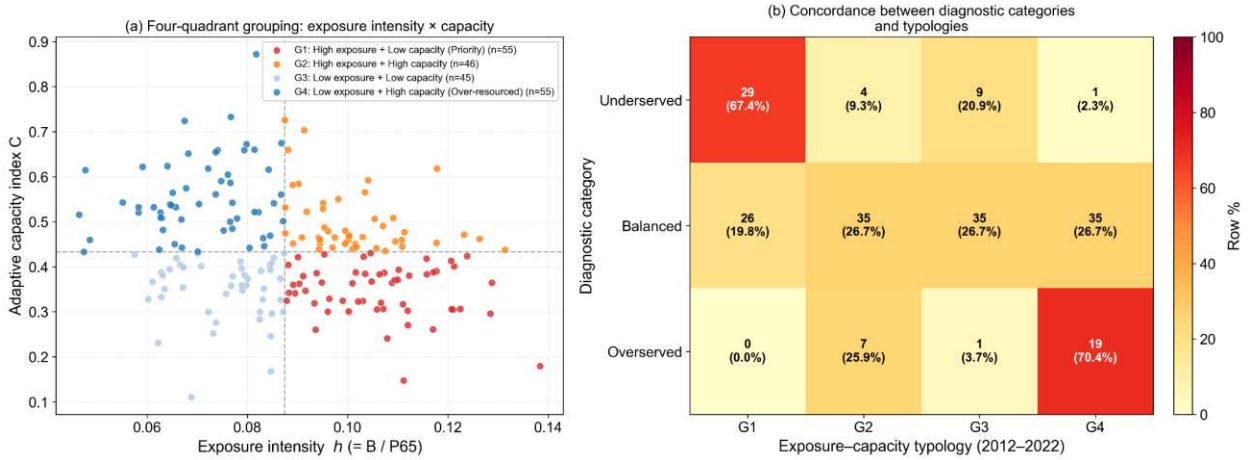


Fig. 5 County typology and concordance with the diagnostic classification.

(a) Counties classified into four quadrants (G1–G4) by median splits of multi-hazard exposure intensity ($h = B/P65$, the ensemble mean across four SSPs and three future periods) and the adaptive-capacity index C (2012–2022); dashed lines mark the medians. Individual counties are plotted, so the within-group dispersion of exposure intensity and capacity is visible directly. (b) Cross-tabulation of the Fig. 4 diagnostic categories (underserved, balanced, overserved) against the G1–G4 typologies; cell values show county counts and row percentages.

Table 2. County typology by multi-hazard exposure intensity and adaptive capacity, with mean indicators and representative counties for each group (G1–G4).

Exposure intensity is the hazard co-occurrence experienced by an average older resident (B/P65); the capacity index C combines bed coverage and fiscal expenditure per older resident (Methods). Bed coverage is beds per 10,000 older residents and fiscal expenditure is in yuan per older resident. Representative counties are the three counties closest to the group median in standardized (h, C) space. Values are group means; the distribution of individual counties in (h, C) space is shown in Fig. 5a.

Typology	Description	Counties (n)	Mean exposure intensity *h*	Mean capacity index C	Mean bed coverage	Mean fiscal exp. per elderly	Representative counties
G1	High exposure intensity, Low capacity (Priority)	55	0.1062	0.345	160.8	39551.5	Mingguang City, Sheyang County, Shangyu District
G2	High exposure intensity, High capacity	46	0.1011	0.499	240.4	72656.4	Linping District, Anji County, Fenghua District
G3	Low exposure intensity, Low capacity	45	0.0754	0.348	182.5	38301.2	Chaohu City, Luhe District, Tongcheng City
G4	Low exposure intensity, High capacity (Over-resourced)	55	0.0708	0.554	384.2	75159.2	Wuzhong District, Jiading District, Minhang District

Marginal benefit is consistently highest in the priority group

Having identified the dually disadvantaged counties, we asked where an additional unit of adaptive capacity would cut residual elderly burden most. Rather than estimating the attenuation of burden by capacity from cross-county variation—which cannot identify an efficacy parameter in the absence of observations linking investment to health outcomes—we specified it. Residual burden is $R_i = h_i \cdot \exp(-\theta C_i)$, so the marginal benefit follows analytically as $MB_i = -\partial R_i/\partial C_i = \theta R_i$ (Methods). We set $\theta = 1$, meaning that raising capacity from the regional minimum to the regional maximum reduces residual burden to 37% of its unadapted level, and tested $\theta \in \{0.5, 1, 2, 3\}$. The choice of θ does not affect the G1 > G4 priority ordering. Evaluated at group means, the ratio of marginal benefit between the priority and over-resourced groups is $(\bar{h}_{G1}/\bar{h}_{G4})\cdot\exp[\theta(\bar{C}_{G4} - \bar{C}_{G1})] = 1.50\exp(0.209\theta)$, which exceeds unity for every $\theta > 0$ and increases monotonically with θ (Methods). The priority group therefore retains the highest marginal benefit at any attenuation strength, not only at the values tested: its advantage is 1.67-fold at $\theta = 0.5$, 1.85-fold at $\theta = 1$ and 2.80-fold at $\theta = 3$ (Supplementary Fig. 7). We report $\theta = 1$ because a stronger attenuation would only enlarge the gap we describe.

Residual burden declines nonlinearly with capacity, so the return on each additional unit falls as capacity rises (Fig. 6a). Because priority counties combine high exposure intensity with low capacity, they occupy the steep segment of the attenuation curve, whereas over-resourced counties sit on its flattened tail (Fig. 6b). Ensemble-mean marginal benefit is 0.075 in G1 and 0.041 in G4—a 1.85-fold gap—with G2 (0.062) and G3 (0.053) in between, and the ordering G1 > G2 > G3 > G4 holds in every scenario (Fig. 6c). Marginal benefit is positive everywhere by construction, so the comparison concerns where returns are largest rather than whether they are positive.

The advantage of the priority group arises less from higher exposure than from its position on the curve. G1 and G2 differ by only 5% in mean exposure intensity (0.106 versus 0.101) but by 22% in mean marginal benefit, because G2 counties sit at substantially higher capacity (mean C = 0.50 versus 0.35). Equity and efficiency therefore coincide for a structural reason: the counties with the least capacity are, by the form of the attenuation function, those where an added unit of capacity removes most burden.

This ranking is stable across emission pathways, though the gap narrows modestly as emissions rise: the G1/G4 ratio declines from 1.91 under SSP1-2.6 to 1.76 under SSP5-8.5, because absolute gains in marginal benefit are somewhat larger in the low-intensity groups. All four typologies peak under SSP3-7.0, consistent with the exposure trajectories in Fig. 2 and Table 1. Directing incremental capacity toward high-intensity, low-capacity counties therefore yields the largest reduction in residual elderly burden under every pathway considered.

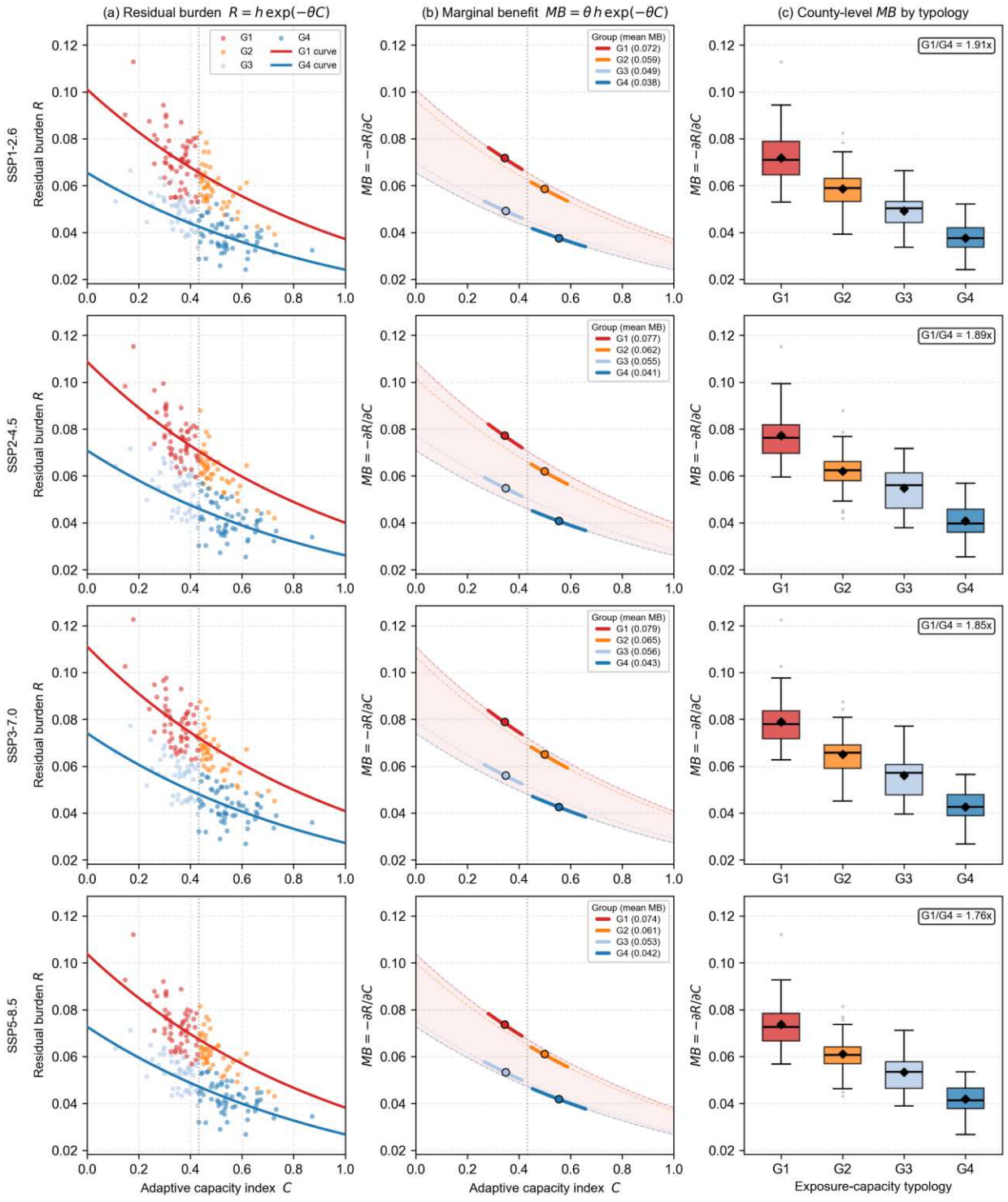


Fig. 6 Attenuation of residual elderly burden by adaptive capacity and the resulting marginal benefit across four SSP scenarios.

(a) Residual burden $R = h\cdot\exp(-\theta C)$ against the adaptive-capacity index C. Points are individual counties coloured by typology; curves show the attenuation function evaluated at the mean exposure intensity of G1 and G4. (b) Marginal benefit $MB = -\partial R/\partial C = \theta R$. Dashed lines give the full function for each

typology; bold segments span the 10th–90th percentile of C observed within that typology; circles mark the group mean (mean C, mean MB). Shading spans the G1–G4 range. (c) Distribution of county-level MB by typology; diamonds mark group means. Rows correspond to SSP1-2.6, SSP2-4.5, SSP3-7.0 and SSP5-8.5. Vertical dotted lines mark the median C.

Mapping marginal benefit confirms that the highest returns concentrate in the dually disadvantaged counties (Fig. 7a). The high-MB cluster coincides with both the exposure-intensity hotspots of Fig. 3 and the underserved counties of Fig. 4b. This priority is robust to the emission trajectory, though not because the gap widens. Marginal benefit rises with emissions in most counties (165 of 201; Fig. 7b), and the increase is smallest in the priority group and largest in the over-resourced group (mean ΔMB = +0.0019 in G1 versus +0.0042 in G4, equivalent to 2.5% and 10.3% of their respective baselines). Exposure intensity therefore converges modestly across typologies under high emissions, narrowing the G1/G4 ratio to 1.76 under SSP5-8.5. The 36 counties where marginal benefit declines lie predominantly along the coast, consistent with the non-monotonic typhoon-wind signal in Fig. 2c. The robustness of the priority ranking therefore rests on invariance rather than on a widening advantage: G1 retains the highest marginal benefit and G4 the lowest under every pathway, and, as shown analytically in Methods, under every positive value of θ (Supplementary Fig. 7). Redirecting incremental investment from over-resourced to underserved counties remains a no-regret strategy—it delivers the largest reduction in residual elderly burden regardless of how emissions evolve—but the size of that advantage is modestly emission-dependent.

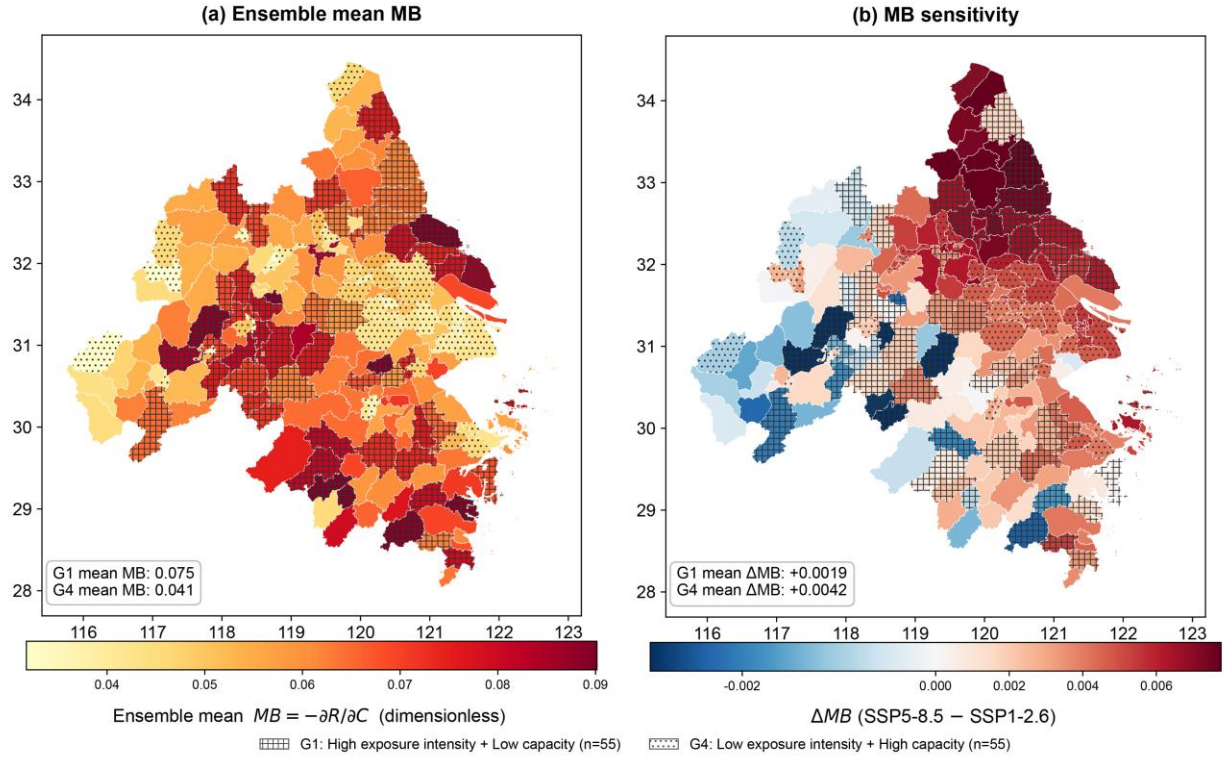


Fig. 7 Marginal benefit of healthcare investment: ensemble priority and emission-pathway sensitivity.

(a) Ensemble-mean marginal benefit MB = −∂R/∂C, averaged over four SSPs and three future periods. MB is dimensionless (Methods). (b) Emission-pathway sensitivity, ΔMB = MB(SSP5-8.5) − MB(SSP1-

2.6); the colour scale is centred on zero. Cross-hatching marks G1 counties (high exposure intensity, low capacity; n = 55) and dotted shading marks G4 counties (low exposure intensity, high capacity; n = 55). θ = 1 throughout.

Discussion

Adaptation priorities for an ageing population cannot be inferred from climate hazard alone. Across the YRDUA, projected elderly multi-hazard exposure intensifies most in several less-developed inland counties, but the planning challenge sharpens only when this exposure is set against healthcare capacity: the counties that face the highest future exposure are frequently those with the lowest hospital-bed coverage per older resident, whereas some lower-exposure counties hold comparatively abundant resources. Crucially, these dually disadvantaged counties are also where each additional unit of investment yields the largest modelled reduction in residual burden[35,36]. This convergence is not visible from a hazard map or a service-supply map alone; it emerges only when exposure, capacity, and marginal return are analysed together. The contribution of EDGE is precisely this integration. It proceeds from measuring population-weighted compound exposure, to diagnosing its mismatch with healthcare capacity, to guiding investment through scenario-specific marginal benefit. This workflow links elderly climate exposure to healthcare equity, and turns risk assessment into a basis for deciding where adaptive capacity is most needed.

The counties that combine high per-resident exposure with low capacity—concentrated in southern Anhui and northern Jiangsu—illustrate a structural rather than incidental pattern. Their elevated ageing rates are driven less by large absolute numbers of older residents than by the sustained out-migration of younger working-age populations, which leaves behind demographically older and economically weaker communities[37–39]. This divergence is visible in the projections, where elderly numbers rise against a declining total population (Supplementary Figs. 4–5). These same communities tend to have limited fiscal capacity and historically thinner healthcare provision, so high exposure and low capacity accumulate in the same places[40–42]. This pattern is the spatial expression of the inverse care law[43], whereby the availability of medical resources varies inversely with the need of the population served, and it stands in clear contrast to the populous Shanghai–Suzhou–Hangzhou core, where large elderly populations coincide with comparatively modest hazard intensification and abundant healthcare resources.

The central implication follows from the nonlinear relationship between healthcare capacity and residual elderly burden[44,45]. Because residual burden declines steeply at low levels of bed coverage and flattens as coverage rises, counties on the steep, under-resourced portion of the curve obtain the greatest reduction in residual burden per unit of added capacity—and these are precisely the high-exposure, low-coverage counties identified in the diagnostic step. Equity and efficiency therefore point in the same direction: the most underserved counties are also where the marginal return is largest. In ensemble-mean terms, marginal benefit is highest in the priority group (G1, mean = 0.075) and lowest in the over-resourced group (G4, mean = 0.041). The ranking is stable across pathways; what varies is the magnitude of the gap, which narrows from 1.91-fold under SSP1-2.6 to 1.76-fold under SSP5-8.5. The robustness of the conclusion lies not in any single scenario, but in the consistent co-location of greatest need and greatest marginal return across the ensemble.

This sub-national finding contrasts with global-scale assessments of exposure inequality[46,47]. At the international level, exposure inequality varies sharply across socioeconomic pathways: it is largest under high-inequality scenarios and smallest under sustainable ones. Within the YRDUA, by comparison, the geography of priority counties is largely insensitive to the emission pathway: the same dually disadvantaged counties remain priorities across all four SSPs, even as the absolute magnitude of exposure shifts. This stability means that reallocating healthcare investment toward underserved, high-exposure counties is effective regardless of how emissions ultimately evolve—a no-regret strategy whose value does not depend on resolving the deep uncertainty of long-term emission trajectories.

These results carry two planning implications. First, for the screening step, equity and efficiency are aligned: G1 counties combine high exposure with low coverage and are defensible first-look priorities even before a marginal-benefit model is applied, which then refines the screening under scenario-specific conditions. Second, the coexistence of lower-intensity, higher-capacity counties with systematically smaller marginal returns indicates that historical patterns of healthcare capacity may not match future climate–health burden[48,49]. This is not an argument for withdrawing essential services from well-resourced counties; rather, it implies that incremental adaptation investment should be evaluated against forward-looking exposure, ageing structure, capacity deficit, and diminishing returns. Such a shift is especially relevant to the YRDUA, where healthcare resources, fiscal capacity, and elderly exposure cross administrative boundaries while investment decisions are typically made within local jurisdictions; the framework can support cross-county priority setting by identifying where local investment carries regional adaptation significance.

Several limitations bound these conclusions. The analysis covers the 201 county-level units of the YRDUA and its findings are specific to this planning entity; whether the same exposure–capacity mismatch characterizes other Chinese urban agglomerations remains to be tested. Healthcare capacity is represented primarily by bed coverage and fiscal indicators, which omit staffing, quality of care, referral capacity, and inter-county patient flows. Capacity is characterized from 2012–2022 records and held fixed against future exposure; this stationarity assumption is a simplification, since both healthcare provision and the fiscal capacity underpinning it will themselves evolve. The marginal-benefit estimate is a dimensionless planning index rather than a causal measure of health outcomes.

These constraints point to clear next steps: incorporating richer capacity dimensions and observed climate-sensitive morbidity where available, and testing whether alternative hazard weights alter the ranking of priority counties. They do not, however, unsettle the central conclusion, which is robust in direction: across the YRDUA, the counties facing the greatest future exposure are also those least able to absorb it, making equity-informed reallocation of healthcare investment both a normative and an operational priority under multiple climate pathways.

Methods

Study area and analytical units

The analysis covers the Yangtze River Delta Urban Agglomeration (YRDUA) as delineated by the 2016 Development Plan for the Yangtze River Delta Urban Agglomeration, which defines the agglomeration as 26 prefecture-level cities across Shanghai, Jiangsu, Zhejiang and Anhui. This

delineation was adopted because regional healthcare provision, fiscal allocation and infrastructure planning in the delta are formulated and reported against this boundary, so the analysis sample corresponds throughout to a single, officially defined planning entity. The county-level unit was adopted as the analytical unit because healthcare supply, fiscal expenditure and administrative planning are reported and implemented at this scale. The final spatial sample comprised 201 county-level units with complete administrative healthcare records for 2012–2022 and full coverage by the climate and population grids.

Climate, population and healthcare data

Future climate information was obtained from CMIP6 Scenario MIP-consistent projections[50,51] and the China 10 km super-resolution daily climate projections with potential-evapotranspiration estimates (SRCPCN10), which provide daily multi-variable fields for 2015–2100 under the SSP pathways from five CMIP6 models[52]. Historical meteorological context was drawn from the China Meteorological Forcing Dataset v2.0 for 1951–2020. The analysis used SSP1-2.6, SSP2-4.5, SSP3-7.0 and SSP5-8.5 across three future windows—2025–2050, 2050–2075 and 2075–2100—relative to a 2015–2025 baseline. Gridded population aged 65 years and older was aligned to the hazard grids and aggregated to counties, following established practice in spatially explicit SSP population-exposure assessment[53–55]. County-level hospital beds, resident population, population aged ≥65 and general public-budget expenditure were compiled from statistical yearbooks and administrative records for 2012–2022, yielding a balanced panel of 201 counties × 11 years. Derived indicators were recomputed from the raw fields rather than taken from the compiled columns: bed coverage (beds per 10,000 residents aged ≥65), ageing rate (population aged ≥65 divided by resident population) and fiscal expenditure per older resident. County-level indicators used in the diagnostic and typology steps are period means over 2012–2022, computed as ratios of period-mean raw quantities to avoid the instability of averaging ratios.

Hazard-index construction

Three climate-hazard components were considered—extreme precipitation, heatwave and typhoon wind—each computed on the gridded climate data before being aggregated to counties using the elderly-population layer. Let *g* denote a grid cell, *d* a day, *y* a year, *s* an SSP pathway and *m* a climate model.

Extreme precipitation hazard was quantified with a graded threshold-exceedance scheme consistent with the national precipitation classification standard (GB/T 28592), so that rarer daily rainfall contributes disproportionately to the score. For daily precipitation *P(g, d), the annual graded precipitation-extreme score was defined as a severity-weighted count:*

$$EP_{g,y,s,m} = \sum_{k=1}^{K} \omega_k \cdot N\left(P_{g,d} \geq \tau_k\right)$$

where $\tau_k \in \{50, 100, 250\}$ mm demarcate the rainstorm, heavy-rainstorm and extraordinary-rainstorm classes, $\omega_k \in \{1, 2, 4\}$ are severity weights increasing with class rarity, $N(\cdot)$ counts qualifying days within year *y*, and $k = 3$. This graded formulation follows the event-frequency logic of the ETCCDI indices while retaining a regionally calibrated intensity interpretation appropriate to monsoonal East Asia[56–58]. To reduce inter-model systematic bias before index construction, daily precipitation from each CMIP6 model was bias-corrected against the reference dataset by quantile mapping over the 2015–2025 calibration window[58].

Heatwave hazard was constructed from daily maximum temperature $T_{max}(g, d)$ using a duration-and-intensity event definition that captures the health-relevant persistence of heat extremes. A heatwave day was identified where T_{max} exceeded the calendar-day 90th-percentile threshold $T_{90}(g)$, derived from the 2015–2025 baseline with a 15-day moving window[59,60]:

$$I_{g,d} = 1\left(T_{g,d}^{max} > T_{90,g}\right)$$

A heatwave event was defined as a run of at least three consecutive heatwave days. For each event e of duration L_e days, the excess-heat magnitude was accumulated as the sum of daily exceedances over the event:

$$M_e = \sum_{d \in e} \left(T_{g,d}^{max} - T_{90,g}\right)$$

The annual heatwave hazard was then taken as the total excess heat accumulated over all qualifying events in year y:

$$HW_{g,y,s,m} = \sum_{e=1}^{n_y} M_e$$

where ny is the number of qualifying events in year y. Because Me is summed over the days of an event, this annual heat load is exactly separable into three properties of the heatwave regime that generate it:

$$HW = n_y \cdot \overline{L} \cdot \overline{I}, \quad \overline{L} = \frac{1}{n_y} \sum_e L_e, \quad \overline{I} = \frac{\sum_e M_e}{\sum_e L_e}$$

that is, the number of events, their mean duration, and the duration-weighted mean daily exceedance. A grid cell therefore attains a high HW through more frequent events, longer events, hotter events, or any combination of the three, and the index deliberately does not distinguish among these routes: cumulative excess-heat metrics of this family predict elderly heat mortality better than counts of threshold-exceeding days, because physiological strain accumulates over a sustained event rather than resetting each day[61,62].

Typhoon-wind hazard was derived in two stages: cyclone-track detection from the model fields, followed by parametric wind reconstruction. Tropical-cyclone centres were identified in each CMIP6 model with an objective feature-tracking algorithm that locates relative-vorticity maxima at 850 hPa exceeding $\zeta_{850} > 3.5 \times 10^{-5}$ s^{-1} [61,62]. For each detected storm, the surface wind field was reconstructed with a parametric radial profile:

$$V(r) = V_{max}\left[\left(\frac{r}{R_{max}}\right)^b \cdot exp\left(1 - \left(\frac{r}{R_{max}}\right)^b\right)\right]^{\frac{1}{2}}$$

where $V(r)$ is the wind speed at radial distance r from the storm centre, V_{max} is the maximum sustained wind, R_{max} is the radius of maximum wind, and b is the Holland pressure-profile shape parameter[63,64]. The

annual typhoon-wind hazard at each grid cell was taken as the maximum reconstructed gust over all storms passing within the influence radius during year y:

$$TW_{g,y,s,m} = \max_{e} V_{g,e}$$

Detection thresholds, the influence radius and the Holland-b parameterization are archived with the analysis code to ensure reproducibility.

Standardization and compound exposure

To render the three hazard components dimensionally comparable, each annual hazard field $X_j(g, y, s, m)$, with $j \in \{\text{EP, HW, TW}\}$, was standardized over all grid cells with positive elderly population within the analysis domain Ω:

$$Z_{j,g,y,s,m} = \frac{X_{j,g,y,s,m} - \mu_j}{\sigma_j}, \quad \mu_j = \frac{1}{|\Omega|}\sum_{g\in\Omega} \overline{X}_{j,g}\,, \quad \sigma_j = \sqrt{\frac{1}{|\Omega|}\sum_{g\in\Omega}\left(\overline{X}_{j,g} - \mu_j\right)^2}$$

where μ_j and σ_j are the domain mean and standard deviation of hazard j. The standardized score was then mapped to a bounded hazard membership on [0,1] through a logistic transform, which suppresses the influence of extreme outliers while preserving monotonicity:

$$S_{j,g,y,s,m} = \frac{1}{1 + exp\left(-Z_{j,g,y,s,m}\right)}$$

The compound multi-hazard co-occurrence index was constructed as a weighted geometric mean of the three membership scores, with equal weights $w_j = 1/3$ in the primary analysis:

$$HI_{g,y,s,m} = \prod_{j\,\in\,\{\text{EP,HW,TW}\}} S_{j,g,y,s,m}^{\,w_j}\,, \quad \sum_j w_j = 1$$

The multiplicative (geometric) form is a compensatory–conjunctive aggregator: unlike an additive index, it returns a high value only when all three hazards are simultaneously elevated and collapses toward zero if any single component is negligible. This makes HI an explicit measure of hazard co-occurrence rather than of a single dominant driver, consistent with the compound-event framework in which concurrent stressors produce impacts exceeding the sum of their marginal effects[65,66].

Population-weighted elderly exposure (pre-adaptation burden) was defined at grid scale and aggregated to county i:

$$B_{g,y,s,m} = HI_{g,y,s,m} \times P_{g,y,s}^{65}$$

$$B_{i,s} = \frac{1}{|Y|}\sum_{y\in Y}\frac{1}{M}\sum_{m=1}^{M}\sum_{g\in i} B_{g,y,s,m}$$

where P_{65} is the projected number of residents aged 65 years and older, $|Y|$ the number of years in an assessment window and M the number of climate models. Relative change was expressed against the

2015–2025 baseline as $B_{var} = (B_{future} - B_{base}) / B_{base}$, with near-zero-baseline counties masked before mapping and a signed-log transform, $\mathrm{sgn}(B_{var}) \cdot \ln(1 + |B_{var}|)$, applied for visualization only.

Because B is a population-weighted aggregate, it scales with the absolute number of older residents and is therefore dominated by county size: across the study region the elderly population spans a 43.5-fold range. Aggregate exposure answers where the greatest numbers of older adults are exposed and is used for the hazard mapping in Figs. 2–3. For the diagnostic, typology and marginal-benefit steps, which concern the adequacy of per-resident provision, we instead use exposure intensity—the hazard co-occurrence experienced by an average older resident in county i:

$$h_{i,s} = B_{i,s} / P65_{i,s}$$

where $P65_{i,s}$ is the projected population aged ≥65 in county i, aggregated over the same grid cells, scenario and assessment window as B. Equivalently, h is the elderly-population-weighted mean of HI over the grid cells of county i, and is therefore bounded on the same [0,1] scale as HI and directly comparable with the per-resident capacity indicators defined below.

Healthcare adaptive capacity and residual burden

Healthcare capacity was treated as an adaptive resource that mitigates burden after exposure, not as a modifier of physical hazard. A composite adaptive-capacity index C_i was constructed for county i from two per-resident indicators—hospital-bed coverage b_i (beds per 10,000 residents aged ≥65) and fiscal expenditure per older resident f_i—each log-transformed to compress the right skew, min–max normalized to [0,1] across the analysis sample, and combined with equal weights:

$$C_i = \frac{1}{2}(\tilde{b}_i + \tilde{f}_i),\ \tilde{b}_i = \mathrm{minmax}[\ln(1 + b_i)],\ \tilde{f}_i = \mathrm{minmax}[\ln(1 + f_i)]$$

so that higher C_i denotes greater healthcare capacity relative to elderly need[67,68]. Two choices warrant comment. First, the ageing rate is excluded from C: it is a measure of need rather than of capacity, and it already enters the analysis twice—through P65 in the exposure term and through the denominator of bed coverage—so including it would triple-count the same demographic signal. Second, fiscal expenditure is expressed per older resident rather than per bed. Expenditure per bed takes the bed count as its denominator and is consequently negatively correlated with bed coverage in this panel (Spearman $\rho = -0.507$, $P = 1.6 \times 10^{-10}$), so the two components would partly offset one another and compress the variance of C; expenditure per older resident is positively associated with bed coverage ($\rho = +0.191$, $P = 0.007$, 95% CI [0.054, 0.321]) and preserves the interpretation of C as "beds per older resident scaled by the fiscal support behind each bed". Normalization constants and all percentile thresholds were computed on the final 201-county analysis sample.

Residual burden R_i—the modelled portion of exposure remaining after adaptive capacity is accounted for—was represented through a capacity-dependent attenuation function $A(C_i) \in (0,1]$ that decreases monotonically with capacity:

$$R_{i,s} = h_{i,s} \times A(C_i),\ A'(C_i) < 0$$

This multiplicative attenuation follows the hazard–vulnerability–capacity formulation in which realized risk is the product of exposure and a capacity-conditioned vulnerability term[71,72]. Crucially, $A(C_i)$

modifies only the health-system-mediated portion of burden and does not alter the physical hazard fields, formalising the premise that hospital beds cannot prevent heatwaves, extreme rainfall or typhoon winds but can reduce their residual health consequences.

Mismatch diagnostics and county typology

Healthcare mismatch was evaluated by comparing the geography of ageing, exposure and bed coverage. Bed coverage across ageing-rate quintiles was compared with the Kruskal–Wallis test and Dunn post-hoc comparisons with Bonferroni adjustment; distributional inequality in bed coverage was summarized with the Gini coefficient and the Lorenz curve; and the monotonic association between ageing rate and bed coverage was assessed with the Spearman rank correlation[69–71]. Two classifications were derived. The diagnostic classification uses healthcare indicators alone: counties with an ageing rate at or above the 75th percentile and bed coverage below the median were labelled underserved (n = 43); counties with an ageing rate at or below the 25th percentile and bed coverage above the 75th percentile were labelled overserved (n = 27); the remainder were labelled balanced (n = 131). The analytical typology classifies counties by median splits of exposure intensity h (ensemble mean over four SSPs and three future windows) and the adaptive-capacity index C, yielding G1 (high intensity, low capacity; n = 55), G2 (high intensity, high capacity; n = 46), G3 (low intensity, low capacity; n = 45) and G4 (low intensity, high capacity; n = 55). The two schemes share bed coverage as an input but differ in their remaining axes, so their agreement is informative but not definitional; concordance is reported as a cross-tabulation rather than as evidence of independent convergence.

Marginal-benefit modelling and sensitivity

The marginal-benefit analysis identifies where an additional unit of adaptive capacity would most reduce residual burden. Rather than estimating the attenuation function from cross-county variation, we specify it. An efficacy parameter cannot be identified from these data: no observations link capacity investment to health outcomes at county scale in this region, so any parameter recovered by regressing burden on capacity across counties would reflect cross-sectional association rather than adaptation efficacy. We therefore adopt an exponential attenuation with a stated parameter:

$$A(C_i) = \exp(-\theta C_i),\ R_{i,s} = h_{i,s} \cdot \exp(-\theta C_i)$$

from which the marginal benefit of additional capacity follows analytically as the negative first derivative:

$$MB_{i,s} = -\frac{\partial R_{i,s}}{\partial C_i} = \theta \cdot h_{i,s} \cdot \exp(-\theta C_i) = \theta \cdot R_{i,s}$$

Marginal benefit is thus proportional to residual burden, is strictly positive, increases with exposure intensity and decreases with capacity, so that counties combining high exposure with low capacity exhibit the largest returns as a structural property of the formulation rather than as an estimated result. No curve fitting, model selection or goodness-of-fit assessment is involved.

We set $\theta = 1$ in the primary analysis, so that $\exp(-\theta) = 0.37$: raising capacity from the regional minimum to the regional maximum reduces residual burden to 37% of its unadapted level. Sensitivity was assessed over $\theta \in \{0.5, 1, 2, 3\}$. The role of θ is analytically transparent. Evaluating MB at group means, the ratio between any two typologies j and k is $(\bar{h}_j/\bar{h}_k)\cdot\exp[\theta(\bar{C}_k - \bar{C}_j)]$, so its logarithm is linear in θ with

slope $\bar{C}_k - \bar{C}_j$. For the priority and over-resourced groups this gives 1.50 exp(0.209θ): the ratio exceeds unity at $\theta \to 0$ and increases monotonically thereafter, so G1 > G4 holds for every $\theta > 0$ rather than only for the values tested. The same expression identifies where intermediate rankings change: G2 exceeds G3 for $\theta < 1.9$ and the order reverses above it, which is the only θ-dependence in the typology ordering (Supplementary Fig. 7). Because exp($-\theta C$) is convex, the group-mean expression approximates the mean of county-level MB to within 2% over the tested range; all reported values are computed county by county. Larger θ widens the G1–G4 gap, so $\theta = 1$ understates rather than overstates the priority advantage relative to any $\theta > 1$.

Because h is a bounded co-occurrence index rather than a count of health events, MB is dimensionless: it expresses the reduction in exposure-weighted residual burden per unit increase in an index that spans [0,1] across the region. It supports ranking counties and comparing typologies within this study and is not an estimate of adverse outcomes averted. Ensemble priority was computed as the four-SSP mean of MB_i, and emission-pathway sensitivity as $\Delta MB_i = MB_i(\text{SSP5-8.5}) - MB_i(\text{SSP1-2.6})$.

Statistics and reproducibility

All analyses were performed in Python 3.12.1 using NumPy 2.3.1, pandas 2.3.1 and SciPy 1.16.0. The analysis sample comprises all 201 county-level units meeting the inclusion criteria defined above (complete administrative healthcare records for 2012–2022 and full coverage by the climate and population grids). Sample size was not statistically predetermined: the sample is the complete population of qualifying units within the 2016 YRDUA delineation, not a draw from it. No unit was excluded after inclusion, and no data points were removed as outliers. Randomization and blinding do not apply to this observational design. All tests are two-sided and evaluated at $\alpha = 0.05$. Exact P values are reported; values below 1×10^{-10} are given as $P < 1 \times 10^{-10}$, because the asymptotic approximations underlying these tests do not support finer resolution in that tail.

Non-parametric procedures were used throughout because the healthcare indicators depart from normality: bed coverage is strongly right-skewed (skewness 2.67, excess kurtosis 8.83; Shapiro–Wilk $W = 0.722$, $P < 1 \times 10^{-10}$), as is fiscal expenditure per older resident (skewness 3.03, excess kurtosis 13.26; $W = 0.720$, $P < 1 \times 10^{-10}$), while the ageing rate departs more modestly but still significantly (skewness 0.72; $W = 0.971$, $P = 3.5 \times 10^{-4}$); $n = 201$ throughout. Log-transformation reduces but does not remove this departure (bed coverage $W = 0.951$, $P = 2.1 \times 10^{-6}$; fiscal expenditure per older resident $W = 0.966$, $P = 8.3 \times 10^{-5}$), and the hypothesized ageing–coverage relation is monotonic rather than linear, so rank-based tests were preferred to their parametric counterparts.

Differences in bed coverage across ageing-rate quintiles were assessed with the Kruskal–Wallis H test with correction for ties (A1–A5; n = 41, 40, 40, 40, 40; $H = 40.84$, d.f. = 4, $P = 2.9 \times 10^{-8}$; $\varepsilon^2 = 0.188$). Quintile boundaries were computed on the 201-county analysis sample. Post-hoc pairwise contrasts used Dunn's test with a tie-corrected rank variance over the single family of 10 quintile pairs, with Bonferroni adjustment of the P values (multiplication by 10, capped at 1); the test was implemented directly rather than through a package, and the code is archived with the analysis scripts. All post-hoc P values reported in the text and in Fig. 4d are Bonferroni-adjusted, and the complete adjusted matrix with the corresponding z statistics is given in Supplementary Table 1.

Monotonic associations were quantified with Spearman's rank correlation coefficient, with P from the two-sided asymptotic t approximation and 95% confidence intervals from the Fisher z transform: ageing rate versus bed coverage ($\rho = -0.470$, $n = 201$, $P < 1 \times 10^{-10}$, 95% CI −0.571 to −0.355); fiscal expenditure per bed versus bed coverage ($\rho = -0.507$, $n = 201$, $P < 1 \times 10^{-10}$, 95% CI −0.603 to −0.396); fiscal expenditure per older resident versus bed coverage ($\rho = +0.191$, $n = 201$, $P = 0.007$, 95% CI 0.054 to 0.321).

Inequality in bed coverage is summarized by the Gini coefficient (Gini = 0.2814; population-weighted Gini = 0.2519) and the Lorenz curve; these are descriptive measures of the full sample and are reported without inferential testing. Group summaries are given as means for the typology indicators in Table 2 and as medians with interquartile range for the quintile comparisons in Fig. 4c; n is stated for every group. Table 2 is a descriptive overview of the four typologies and is not used inferentially; the dispersion of individual counties within each group is shown directly by the scatter of Fig. 5a. Box plots show the median (centre line), the interquartile range (box) and whiskers extending to 1.5 × IQR, with individual counties overlaid.

No inferential test is applied to the marginal-benefit results. MB is a deterministic function of exposure intensity and capacity given a stated θ, evaluated for the complete set of 201 counties, so differences between typologies in Figs. 6–7 are properties of the population rather than estimates carrying sampling error, and are reported as descriptive comparisons without P values. Robustness is instead established by invariance: the G1 > G4 ordering holds under all four SSP pathways, all three future windows, all five CMIP6 models and, analytically, for every $\theta > 0$.

Data Availability

The climate projection data used in this study are available from the National Tibetan Plateau Data Center as SRCPCN10 (DOI: 10.11888/Atmos.tpdc.302144). The historical meteorological forcing data are available from the National Tibetan Plateau Data Center as CMFD v2.0 (DOI: 10.11888/Atmos.tpdc.302088). The county-level healthcare, fiscal, and administrative datasets analysed during the current study are subject to license restrictions and thus are not publicly available. However, processed analysis-ready tables and data are available from the corresponding author upon reasonable request.

References

1. Pörtner, H.-O. *et al.* Climate change 2022: Impacts, adaptation and vulnerability. (2022).
2. Zhao, L. China’s aging population: A review of living arrangement, intergenerational support, and wellbeing. *Health Care Sci.* **2**, 317–327 (2023).
3. Cai, W. *et al.* The 2024 China report of the Lancet Countdown on health and climate change: launching a new low-carbon, healthy journey. *Lancet Public Health* **9**, e1070–e1088 (2024).

4. Hartinger, S. M. *et al.* The 2025 Lancet Countdown Latin America report: moving from promises to equitable climate action for a prosperous future. *Lancet Reg. Health - Am.* **52**, 101276 (2025).
5. Romanello, M. *et al.* The 2023 report of the lancet countdown on health and climate change: The imperative for a health-centred response in a world facing irreversible harms. *The Lancet* **402**, 2346–2394 (2023).
6. Zhang, Y., Yao, R., Zhu, Z., Jin, H. & Zhang, S. Spatiotemporal evolution of population exposure to multi-scenario rainstorms in the yangtze river delta urban agglomeration. *J. Geogr. Sci.* **34**, 654–680 (2024).
7. Ali, J. Assessing multi-hazard risks and impacts of compound climate and weather extreme events for socio-economic risk management. (2025).
8. Foshag, K. *et al.* How to assess the needs of vulnerable population groups towards heat-sensitive routing? An evidence-based and practical approach to reducing urban heat stress. *Erdkunde* 1–34 (2024).
9. Moore, C. L. & Cong, Z. Climate change, older adults, and people with chronic illness. in *Climate Change and Disability* 85–96 (Elsevier, 2026).
10. Bell, M. L., Gasparrini, A. & Benjamin, G. C. Climate change, extreme heat, and health. *N. Engl. J. Med.* **390**, 1793–1801 (2024).
11. Liu, J. *et al.* Heat exposure and cardiovascular health outcomes: A systematic review and meta-analysis. *Lancet Planet. Health* **6**, e484–e495 (2022).
12. Xu, Z. Increased risk of cardiopulmonary mortality during hot weather: Well-designed health impact assessments to inform heat adaptation strategies. *Lancet Reg. Heal.* **46**, (2024).
13. Yadav, A. Climate extremes: Heatwaves, droughts, heavy rainfall and hurricanes. *CLIMATOLOGY* 102.
14. Lindsay, S., Hsu, S., Ragunathan, S. & Lindsay, J. The impact of climate change related extreme weather events on people with pre-existing disabilities and chronic conditions: A scoping review. *Disabil. Rehabil.* **45**, 4338–4358 (2023).

15. Gao, S. & Wang, Y. Anticipating older populations' health risk exacerbated by compound disasters based on mortality caused by heart diseases and strokes. *Sci. Rep.* **13**, 16810 (2023).

16. Prina, M. *et al.* Climate change and healthy ageing: An assessment of the impact of climate hazards on older people. *J. Glob. Health* **14**, 04101 (2024).

17. Tipaldo, J. F., Balk, D. & Hunter, L. M. A framework for ageing and health vulnerabilities in a changing climate. *Nat. Clim. Change* **14**, 1125–1135 (2024).

18. Harrington, L. J. & Otto, F. E. Underestimated climate risks from population ageing. *Npj Clim. Atmos. Sci.* **6**, 70 (2023).

19. Xu, P. *et al.* An explainable percolation-based clustering framework for China's transport carbon emissions analysis. *GIScience Remote Sens.* **63**, 2677263 (2026).

20. Nijhuis, S., Sun, Y. & Lange, E. Introduction: Adaptive urban transformation in the pearl river delta, China. in *Adaptive Urban Transformation: Urban Landscape Dynamics, Regional Design and Territorial Governance in the Pearl River Delta, China* 3–19 (Springer, 2023).

21. Aftab, H., Kumari, N. & Faridi, R. A. Assessing and predicting the impact of urban expansion on land surface temperature and urban heat island intensity in noida. *Discov. Cities* **3**, 75 (2026).

22. Ridder, N. N., Ukkola, A. M., Pitman, A. J. & Perkins-Kirkpatrick, S. E. Increased occurrence of high impact compound events under climate change. *Npj Clim. Atmos. Sci.* **5**, 3 (2022).

23. Tabari, H. & Willems, P. Global risk assessment of compound hot-dry events in the context of future climate change and socioeconomic factors. *Npj Clim. Atmos. Sci.* **6**, 74 (2023).

24. Yang, X., Li, H., Zhang, J., Niu, S. & Miao, M. Urban economic resilience within the yangtze river delta urban agglomeration: Exploring spatially correlated network and spatial heterogeneity. *Sustain. Cities Soc.* **103**, 105270 (2024).

25. Zhu, H. *et al.* Spatiotemporal dynamics and driving forces of land urbanization in the yangtze river delta urban agglomeration. *Land* **11**, 1365 (2022).

26. Typhoon dolphin: More than a million people evacuated in China as record rainfall dumped on shanghai | extreme weather | the guardian. https://www.theguardian.com/world/2026/aug/10/typhoon-dolphin-china-shanghai-flooding-evacuations.

27. Organization, W. H. *Operational Framework for Building Climate Resilient Health Systems*. (World Health Organization, 2015).

28. Higuera Roa, O. *et al.* Challenges and opportunities in climate risk assessment: Future directions for assessing complex climate risks. *Environ. Res. Lett.* **20**, 053003 (2025).

29. Byrne, E. & Heywood, A. Use of routine health information systems data in developing and monitoring district and facility health plans: A scoping review. *BMC Health Serv. Res.* **23**, 1049 (2023).

30. Dokken, D. 11 — human health: Impacts, adaptation, and co-benefits. *Hum. Health*.

31. Hosseinzadehtalaei, P., Hamdi, R., Moradkhani, H., Termonia, P. & Tabari, H. Inequality in human exposure to future climate extremes. *Nat. Commun.* **16**, 8058 (2025).

32. Zhang, M. *et al.* Climate adaptation investments: Short-term shocks and long-term effects of temperature variation on air conditioning adoption. *Sustain. Cities Soc.* **108**, 105493 (2024).

33. Marlier, M. E., Connolly, R., Ma, Y., Jerrett, M. & Benmarhnia, T. Compound climate exposures and public health: A synthesis of research and future directions. *Annu. Rev. Public Health* **47**, (2025).

34. Dinh, N. T. T., Tran, J. & Hensher, M. Measuring and valuing the health co-benefits of climate change mitigation: A scoping review. *Lancet Planet. Health* **8**, e402–e409 (2024).

35. Cheng, E. *et al.* Neighborhood and individual socioeconomic disadvantage and survival among patients with nonmetastatic common cancers. *JAMA Netw. Open* **4**, e2139593 (2021).

36. Evans, G. W. & Kim, P. Multiple risk exposure as a potential explanatory mechanism for the socioeconomic status–health gradient. *Ann. N. Y. Acad. Sci.* **1186**, 174–189 (2010).

37. Wu, L., Huang, Z. & Pan, Z. The spatiality and driving forces of population ageing in China. *Plos One* **16**, e0243559 (2021).

38. Bodvarsson, Ö. B., Hou, J. W. & Shen, K. Aging and migration: Micro and macro evidence from China. *Front. Econ. China* **11**, 548 (2016).

39. Chen, M., Lloyd, C. J. & Yip, P. S. Growing rich without growing old: The impact of internal migration in China. *Asian Popul. Stud.* **16**, 183–200 (2020).

40. Dong, X. & Wang, Y. The geography of healthcare: Mapping patient flow and medical resource allocation in China. *Econ. Hum. Biol.* **55**, 101431 (2024).

41. Jia, P. *et al.* Inequalities of spatial primary healthcare accessibility in China. *Soc. Sci. Med.* **314**, 115458 (2022).

42. Yang, C., Huang, J. & Yu, J. Inequalities in resource distribution and healthcare service utilization of long-term care in China. *Int. J. Environ. Res. Public. Health* **20**, 3459 (2023).

43. Cookson, R., Doran, T., Asaria, M., Gupta, I. & Mujica, F. P. The inverse care law re-examined: A global perspective. *The Lancet* **397**, 828–838 (2021).

44. Zhang, X. *et al.* Factors that dynamically affect provincial incidences of catastrophic health expenditure among middle-aged and elderly Chinese population-transition of disease financial risk protection from global to local. *BMC Geriatr.* **22**, 759 (2022).

45. Shin, S. H. & Ji, H. Health risks of natural hazards and resilience resources: Evidence from a US nationwide longitudinal study. *Soc. Sci. Med.* **281**, 114110 (2021).

46. Zhou, Z. *et al.* Global increase in future compound heat stress-heavy precipitation hazards and associated socio-ecosystem risks. *Npj Clim. Atmos. Sci.* **7**, 33 (2024).

47. Falchetta, G., De Cian, E., Sue Wing, I. & Carr, D. Global projections of heat exposure of older adults. *Nat. Commun.* **15**, 3678 (2024).

48. Liao, S. *et al.* Temperature-related hospitalization burden under climate change. *Nature* **644**, 960–968 (2025).

49. Bi, P., Shi, X.-M. & Liu, Q.-Y. Climate change and population health research in China: Knowledge gaps and further directions. *Adv. Clim. Change Res.* **11**, 273–278 (2020).

50. Van Vuuren, D. P. *et al.* The scenario model intercomparison project for CMIP7 (ScenarioMIP-CMIP7). *Geosci. Model Dev.* **19**, 2627–2656 (2026).

51. Eyring, V. *et al.* Overview of the coupled model intercomparison project phase 6 (CMIP6) experimental design and organization. *Geosci. Model Dev.* **9**, 1937–1958 (2016).

52. Zhang, F., Li, X., Wang, X., Tan, M. & Xin, L. China 10 km super-resolution daily climate projections with potential evapotranspiration estimates (2015-2100)(SRCPCN10). *Natl. Tibet. PlateauThird Pole Environ. Data Cent.* **10**, (2025).

53. He, J. *et al.* China meteorological forcing dataset v2. 0 (1951–2020). *Natl. Tibet. PlateauThird Pole Environ. Data Cent.* (2024).

54. Chen, S. *et al.* Updating global urbanization projections under the shared socioeconomic pathways. *Sci. Data* **9**, 137 (2022).

55. Olén, N. B. & Lehsten, V. High-resolution global population projections dataset developed with CMIP6 RCP and SSP scenarios for year 2010–2100. *Data Brief* **40**, 107804 (2022).

56. Alexander, L. V. *et al.* Global observed changes in daily climate extremes of temperature and precipitation. *J. Geophys. Res. Atmos.* **111**, 2005JD006290 (2006).

57. Rehana, S., Yeleswarapu, P., Basha, G. & Munoz-Arriola, F. Precipitation and temperature extremes and association with large-scale climate indices: An observational evidence over India. *J. Earth Syst. Sci.* **131**, 170 (2022).

58. Reji, M. J. K., Varikoden, H. & Vellore, R. K. Assessment of seasonal and extreme rainfall over kerala using bias-corrected high-resolution climate models: Historical and future changes. *Clim. Dyn.* **64**, 290 (2026).

59. Tan, F., Liu, R., Wu, M., Chen, J. & Ye, Z. Drought-heatwave compound events in China: Long-term changes, regional drivers, and rising event probability. *J. Geophys. Res. Atmos.* **131**, e2026JD046972 (2026).

60. Adeyeri, O. E. *et al.* Coupled climate–land-use interactions modulate projected heatwave intensification across africa. *Commun. Earth Environ.* **7**, 85 (2026).

61. Fu, Z.-H., Zhan, R., Zhao, J., Yamada, Y. & Song, K. Future projections of multiple tropical cyclone events in the northern hemisphere in the CMIP6-HighResMIP models. *Geophys. Res. Lett.* **50**, e2023GL103064 (2023).

62. Han, X. *et al.* Physics-guided score-based diffusion for 3D reconstruction of tropical cyclones from sparse observations. *Npj Clim. Atmos. Sci.* (2026).

63. Cronin, T. W. An analytic model for tropical cyclone outer winds. *Geophys. Res. Lett.* **50**, e2023GL103942 (2023).

64. Sheng, C. & Hong, H. P. Assessing holland's wind pressure profile parameters used for tropical cyclone wind field modelling. *J. Wind Eng. Ind. Aerodyn.* **245**, 105650 (2024).

65. Stalhandske, Z. *et al.* Global multi-hazard risk assessment in a changing climate. *Sci. Rep.* **14**, 5875 (2024).

66. Gohari, A., Saboori, M., Ghadimi, S. & Torabi Haghighi, A. A multivariate framework for assessing compound agroclimatic extremes across europe. *Commun. Earth Environ.* (2026).

67. da Silva, A. C. B., dos Reis, D. R., Libório, M. P., Mannan, H. & Nobre, C. N. A composite indicator of anxiety and depression signs in children and adolescents of low-and middle-income countries: A subjective-objective multidimensional approach. *Child Indic. Res.* 1–40 (2026).

68. Lu, F. *et al.* Comparison of the predictive value of intrinsic capacity and comorbidity on adverse health outcome in community-dwelling older adults. *Geriatr. Nur. (Lond.)* **50**, 222–226 (2023).

69. Behzadifar, M. *et al.* Assessing equity in the distribution of hospital beds in lorestan, western iran: A regional analysis. *J. Prev. Med. Hyg.* **65**, E449 (2024).

70. Wang, Z., Dong, L., Xing, X., Liu, Z. & Zhou, Y. Disparity in hospital beds' allocation at the county level in China: An analysis based on a health resource density index (HRDI) model. *BMC Health Serv. Res.* **23**, 1293 (2023).

71. Song, C. *et al.* Revealing spatiotemporal inequalities, hotspots, and determinants in healthcare resource distribution: Insights from hospital beds panel data in 2308 Chinese counties. *BMC Public Health* **24**, 423 (2024).

Author Contributions

Qi Wu: Methodology, Software, Formal analysis, Investigation, Data curation, Visualization, Writing – original draft.

Peijun Lu: Conceptualization, Supervision, Project administration, Resources, Writing – review & editing.

Shun Huang: Investigation, Writing – original draft.

Wei Wang: Investigation, Visualization.

Mingjing Ding: Investigation, Visualization.

All authors read and approved the final manuscript.

Competing interests

The authors declare no competing interests.

Acknowledgements

This research was supported by the National Natural Science Foundation of China (grant numbers: 5251101668), the China Postdoctoral Science Foundation (grant numbers: GZC20251107, 2025M771604), and the High-Level Talent Scientific Research Startup Funding Project of Anhui Institute of Information Technology (grant number: rckj2026A023), and the Humanity and Social Science Research Project of the Anhui Educational Committee (2024AH052355). The funders played no role in study design, data collection, analysis and interpretation, or writing of this manuscript.

Supplementary Files

This is a list of supplementary files associated with this preprint. Click to download.

- Supplementaryfinal.zip